**Proceedings of the 10th International Pipeline Conference**
**IPC2014**
**September 29 - October 3, 2014, Calgary, Alberta, Canada**

# IPC2014-33225

# DESIGN OF THE FULL SCALE EXPERIMENTS FOR THE TESTING OF THE TENSILE STRAIN CAPACITY OF X52 PIPES WITH GIRTH WELD FLAWS UNDER INTERNAL PRESSURE AND TENSILE DISPLACEMENT

**Celal Cakiroglu**
Department of Civil and Environmental Engineering,
University of Alberta
Edmonton, Alberta, Canada

**Samer Adeeb**
Department of Civil and Environmental Engineering,
University of Alberta
Edmonton, Alberta, Canada

**J. J. Roger Cheng**
Department of Civil and Environmental Engineering,
University of Alberta
Edmonton, Alberta, Canada

**Millan Sen**
Enbridge Pipelines Inc.
Edmonton, Alberta, Canada

## ABSTRACT

Pipelines can be subjected to significant amounts of tensile forces due to geotechnical movements like slope instabilities and seismic activities as well as due to frost heave and thaw cycles in arctic regions. The tensile strain capacity ($\varepsilon_t^{crit}$) of pipelines is crucial in the prediction of rupture and loss of containment capability in these load cases. Currently the Oil and Gas Pipeline Systems code CSA Z662-11 0 contains equations for the prediction of $\varepsilon_t^{crit}$ as a function of geometry and material properties of the pipeline. These equations resulted from extensive experimental and numerical studies carried out by Wang et al [2]-[6] using curved wide plate tests on pipes having grades X65 and higher. Verstraete et al 0 conducted curved wide plate tests at the University of Ghent which also resulted in tensile strain capacity prediction methods and girth weld flaw acceptability criteria. These criteria are included in the European Pipeline Research Group (EPRG) Tier 2 guidelines. Furthermore Verstrate et al 0 introduced a pressure correction factor of 0.5 in order to include the effect of internal pressure in the tensile strain capacity predictions in a conservative way. Further research by Wang et al with full scale pipes having an internal pressure factor of 0.72 also showed that $\varepsilon_t^{crit}$ decreases in the presence of internal pressure [10]-[15]. In their work, Wang et al presented a clear methodology for the design of full scale experiments and numerical simulations to study the effect of internal pressure on the tensile strain capacity of pipes with girth weld flaws [10]-[15]. However, there has been limited testing to enable a precise understanding of the tensile strain capacity of pipes with grades less than X65 as a function of girth weld flaw sizes and the internal pressure.

In this paper the experimental setup for the testing of grade X52 full scale specimens with 12" diameter and ¼" wall thickness is demonstrated. In the scope of this research 8 full scale specimens will be tested and the results will be used to formulate the tensile strain capacity of X52 pipes under internal pressure. The specimens are designed for the simultaneous application of displacement controlled tensile loading and the internal pressure. Finite element analysis is applied in the optimization process for the sizes of end plates and connection elements. Also the lengths of the full scale specimens are determined based on the results from finite element analysis. The appropriate lengths are chosen in such a way that between the location of the girth weld flaw and the end plates uniform strain zones could be obtained. The internal pressure in these experiments is ranging between pressure values causing 80% SMYS and 30% SMYS hoop stress. The end plates and connection elements of the specimens are designed in such a way that the tensile displacement load is applied with an eccentricity of 10% of the pipe diameter with the purpose of increasing the magnitude of tensile strains at the girth weld flaw location.

The results of two full scale experiments of this research program are presented. The structural response from the experiments is compared to the finite element simulation. The remote strain values of the experiment are found to be higher than the $\varepsilon_t^{crit}$ values predicted by the equations in 0.

## NOMENCLATURE

| | |
|---|---|
| $\varepsilon_t^{crit}$ | Tensile strain capacity |
| $\delta$ | Apparent crack-tip opening displacement (CTOD) toughness [mm] |

| | |
|---|---|
| $\eta$ | Ratio of defect height to pipe wall thickness |
| $\lambda$ | Ratio of yield strength to tensile strength (Y/T) |
| $\xi$ | Ratio of defect length to pipe wall thickness |
| $a$ | Defect height for surface –breaking defect [mm] |
| $2a$ | Defect height for buried defect [mm] |
| $2c$ | Defect length [mm] |
| $t$ | Pipe wall thickness [mm] |
| OD | Outer diameter of the pipe |
| SMYS | Specified minimum yield strength |
| $\nu$ | Poisson' s ratio |
| E | Modulus of elasticity |
| $\sigma_h$ | Hoop stress |
| $\sigma_l$ | Longitudinal stress |
| $\varepsilon_h$ | Hoop strain |
| $\varepsilon_l$ | Longitudinal strain |
| $p_i$ | Internal pressure |
| CMOD | Crack mouth opening displacement |

## INTRODUCTION

Steel pipelines have proven to be the most efficient form of oil and natural gas transportation from the remote locations of source like the sub-Arctic region of North America to the location of consumption. Due to temperature fluctuations and freezing/thawing cycles of the permafrost significant tensile forces may be applied on the pipes. These forces cause longitudinal strains due to differential settlement which can exceed the tensile strain capacity ($\varepsilon_t^{crit}$) of the pipe. Also geotechnical forces caused by slope instability or seismic activity can also cause the tensile strain capacity to become exceeded. Girth welds are the parts of a pipeline which are most likely to experience crack propagation and reduced tensile strain capacity because of the high likelihood of welding flaws. In the CSA Z662-11 code 0 girth weld flaws are categorized as surface flaws (Figure 1) and buried flaws. In 0 two sets of equations describe the relationship between girth weld flaw size, material properties and $\varepsilon_t^{crit}$ for both of these flaw types. These equations are developed based on the extensive research of Wang et al [2]-[6].

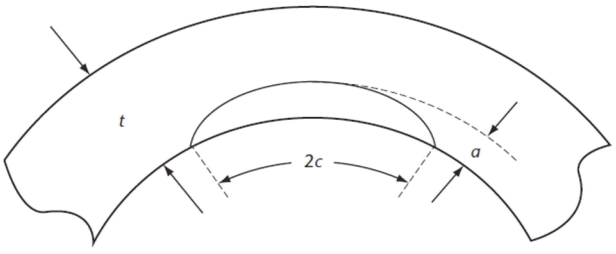


**Figure 1: A planar surface-breaking defect in the pipe wall0**

$$\varepsilon_t^{crit} = \delta^{2.36-1.58\lambda-0.10\xi\eta}(1+16.1\lambda^{-4.45})(-0.157+0.239\xi^{-0.241}\eta^{-0.315}) \quad (1)$$

$$\varepsilon_t^{crit} = \varepsilon_t^{crit}(\delta,\xi,\eta,\lambda) \quad (2)$$

In the scope of this paper we are dealing with the effect of surface type girth weld flaws on the tensile strain capacity. In order to investigate this effect, a flaw is machined into the heat affected zone (HAZ) of the pipe since this location has less material strength compared to the girth weld itself and the rest of the pipe base metal.

In our previous work 0 it was found that for the case of surface flaw, the flaw depth has the greatest effect on $\varepsilon_t^{crit}$ compared to the other parameters in Eq. (1) and Eq. (2). In this experimental program the variation of $\varepsilon_t^{crit}$ with respect to flaw depth $(\eta \cdot t)$ and flaw length $(\xi \cdot t)$ is investigated for X52 pipe. The study of the effect of internal pressure on $\varepsilon_t^{crit}$ is a major component of the research program. The equations currently available in CSA code for the prediction of $\varepsilon_t^{crit}$ are developed based on curved wide plate tests. Therefore it is beneficial to analyze the variation of $\varepsilon_t^{crit}$ at different internal pressure levels. In this paper the experimental setup and the preliminary analyses for different experimental components are elaborated. Also the results of the first full scale experiment are presented.

## 1. DESIGN OF THE FULL SCALE EXPERIMENT

This section explains the general design process of the full scale specimen as well as the details of the preliminary numerical analysis. Based on the estimated forces acting on the specimen, proper dimensions are determined for the end plates. Also this section describes the test setup and the flaw cutting procedure schematically.

The test specimens are cut out of the Norman Wells pipelines NPS 12, grade X52 with nominal wall thickness of 6.91mm. NPS 12 has an outside diameter of 324mm (12.75"), while X52 has a specified minimum yield strength (SMYS) of 359MPa (52KSI). Given those values, the internal pressures corresponding to 80% SMYS and 30% SMYS are given by the Barlow formula as 12.25MPa (1777PSI) and 4.59MPa (666PSI) respectively.

In the scope of this project a total of 8 full scale experiments (Table 1) are planned. Two of these tests are covered in this paper. The experimental setup (Figure 13, Figure 15) mainly consists of a 72" long pipe (NPS 12) having a girth weld in its mid-section being tested in an MTS machine under tensile displacement, in the presence of internal pressure and a flaw machined into the heat effected zone. The flaw depths are chosen to be either 25% or 50% of the nominal wall thickness.

**Table 1: Proposed test matrix**

| Test number | Specimen Length | Internal pressure (% SMYS) | Flaw length [mm] | Flaw depth [mm] |
|---|---|---|---|---|
| 1 | 72” | 80 | 50 | 1.7 |
| 2 | 72” | 30 | 50 | 1.7 |
| 3 | 72” | 80 | 50 | 3.4 |
| 4 | 72” | 30 | 50 | 3.4 |
| 5 | 48” | 80 | 150 | 1.7 |
| 6 | 48” | 10 | 150 | 1.7 |
| 7 | 48” | 80 | 150 | 3.4 |
| 8 | 48” | 30 | 150 | 3.4 |

### 1.1 PRELIMINARY FINITE ELEMENT ANALYSIS

In this section the details of a preliminary finite element model of the full scale specimen are elaborated. This model is used for the estimation of the expected forces that the end plates undergo during the experiment as well as providing an estimation of the expected strain distribution on the pipe during the experiment. For this purpose 12.25MPa (80% SMYS hoop stress) internal pressure as well as eccentric tensile displacement are applied in consecutive load steps in the simulation software “Abaqus”. For this preliminary model, we did not simulate the crack as due to the small size of the crack in tests 1 and 2, we expect that the crack will not affect the global behavior of the pipe. The pipe geometry is discretized using 4 node shell elements with reduced integration (S4R). Symmetry was used, so, only one quarter of the pipe was simulated (Figure 2). The end plate was simulated using shell elements that were glued to the end of the pipe. The material behaviour of the pipe base metal is modelled based on the experimental true stress – plastic strain curves of specimens taken in the longitudinal direction (Figure 3).

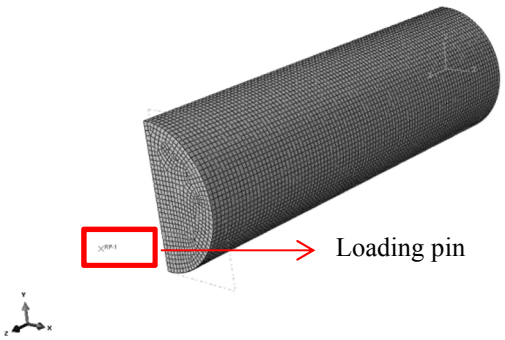


**Figure 2: Finite element mesh showing the end plate, the pipe and the loading pin.**

In this finite element model the end plate which is welded to the pipe base metal and the fixture plate which has the tongue part (Figure 13) are modeled as a single plate having 70 mm thickness. However in the experiment these two plates are connected to each other with 14 bolts. The material and geometric properties listed in Table 2 are used throughout the finite element model.

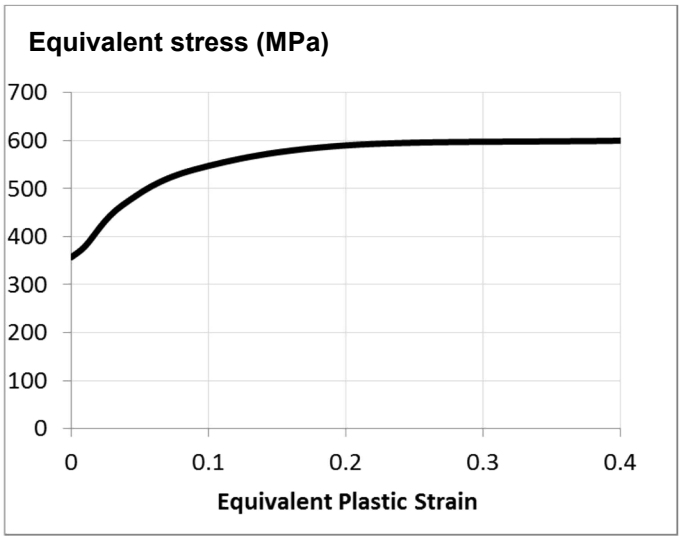


**Figure 3: Plastic material response of the pipe base metal**

**Table 2: Material properties of the pipe base metal and the geometric parameters**

| | |
|---|---|
| Modulus of Elasticity [MPa] | 200000 |
| Yield Strength [MPa] | 360 |
| Ultimate strength [MPa] | 600 |
| Pipe outer diameter (OD) [mm] | 324 |
| Actual Pipe wall thickness (t) [mm] | 6.95 |
| Pipe half-length | 3-OD |

In order to determine a proper wall thickness value to be used in the numerical models, the pipe wall thickness is measured in random locations of the pipe. In total 53 measurements are made. The outlier data which lies 3 standard deviations or more away from the average value is replaced with the average wall thickness. The histogram in Figure 4 shows the frequency of different wall thickness ranges.

According to this histogram a substantial part of the wall thickness measurements fall into the range between 6.9 mm and 7.0 mm. Therefore the average of these two values (6.95 mm) is used as wall thickness in the finite element analysis.

After the application of the 12.25MPa internal pressure in the first load step, in the second load step 85 mm displacement is applied on a rigid point in the middle of the tongue hole in a direction parallel to the pipe longitudinal axis. In the experimental setup this tongue slides into a yoke and a pin connects the tongue to the yoke building a so called pin- yoke assembly (Figure 5). Therefore in the consecutive parts of this text the rigid point at the center of the tongue hole is referred to as the loading pin.

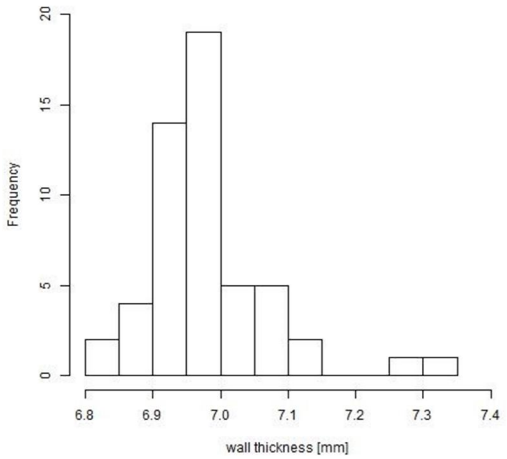


**Figure 4: Frequency distribution of the wall thickness**

In order to transfer the forces acting on the loading pin to the outer surface of the end plate, in the Abaqus finite element model a rigid point tie constraint is defined between the loading pin and a surface on the end plate which has the same size as the base surface of the tongue. In this way the effect of applying longitudinal displacement to the loading pin on the end plate is simulated (Figure 2).

Due to the eccentricity of the tensile displacement (0.1-OD) the end plate rotates throughout the experiment. In order to simulate the effect of this rotation all degrees of freedom of the end plate is constrained except the rotation and axial displacement.

### 1.2 END PLATE DESIGN

The end plate is designed based on the results of the preliminary finite element simulation. In the geometry optimization process a feedback control approach is adopted as illustrated in Figure 6.

In Figure 6, RF denotes the reaction force at the loading pin. The total tensile force applied on the end plate is used to design a bolted connection between the pipe end plate and another connection plate. For this purpose the maximum reaction force expected if the pipe cross section reaches its ultimate strength of 590MPa is equal to 4161kN. The maximum allowable tensile stress for 1 inch (25.8mm) diameter ASTM A490 bolts is equal to 1040MPa. The factored tensile force due to the applied tension and bending per bolt is required to be less than the specified maximum force:

$$f_t = (f_t)_T + (f_t)_{BM} = \frac{\sum RF}{n \cdot A_b} + \frac{\sum RF \cdot e \cdot c}{I} < 1040\ MPa$$

where $(f_t)_T$ and $(f_t)_{BM}$ are the tensile stresses due to tension and bending moment respectively. $A_b$ is the cross section area of one bolt and $n$ is the number of bolts. $\sum RF$ is the total eccentric force acting on the end plate, $e$ is the amount of eccentricity, $c$ is the distance from the pipe axis to the center of the most distant bolt and $I$ is the total moment of inertia of the bolt cross section areas. By choosing $n = 14$, the chosen bolt satisfies the above requirement.

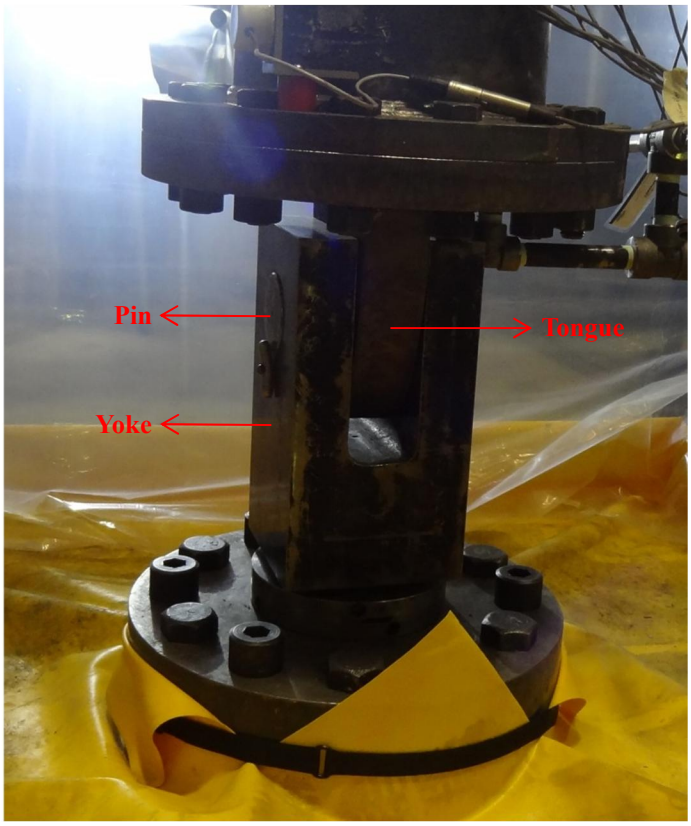


**Figure 5: Pin-yoke assembly connected to the tongue**

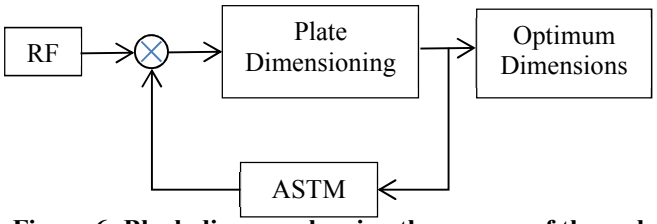


**Figure 6: Block diagram showing the process of the end plate geometry optimization**

### 1.3 HIGH - LOW MISALIGNMENT AT THE GIRTH WELD

In the process of creating the high-low misalignment profile of the full-scale specimens a 3D laser scanner is utilized. The surface geometry which is captured by the laser scanner is analyzed using the reverse engineering software Geomagic. In this procedure the 3D surface geometry of the girth weld location is compared with a perfect cylinder having the same average diameter as the scanned pipe. This average diameter value can be obtained in Geomagic as the diameter of the best

fit cylinder to the scanned pipe surface. Once the scanned girth weld area and the imported perfect cylinder are overlapped, the 3D comparison algorithm of Geomagic created a colour map (Figure 7) which shows the deviation of the scanned surface from the perfect cylinder in millimeters at each point of the scanned surface. In the colour map of Figure 7 shades of green and blue indicate the scanned surface being underneath the surface of the perfect cylinder and the shades of yellow and red indicate the scanned pipe surface being over the perfect cylinder surface. This colour convention can be clearly recognized from the colour of the girth weld location. This location has a dark red colour since the girth weld middle line has substantially greater diameter than the perfect cylinder.

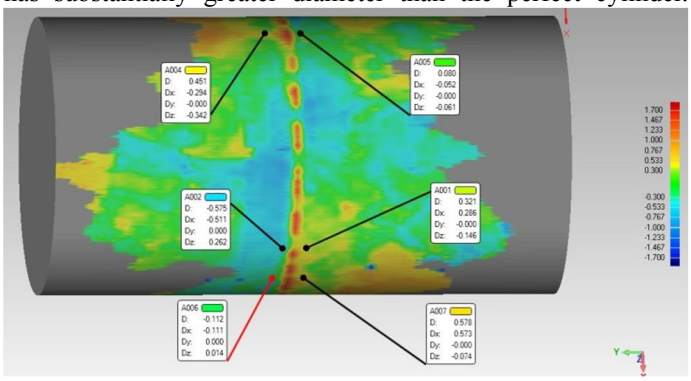

**Figure 7: Determination of the maximum high-low misalignment**

By observing the colour map of Figure 7, three locations of major deviation could be identified. The annotations in Figure 7 show the deviations of the scanned surface from the perfect cylinder on both sides of the girth weld at these major deviation zones. In these annotations the letters $D_x, D_y, D_z$ show the deviations between two surfaces in $x, y$ and $z$ directions respectively and the letter $D$ shows the magnitude of the deviation at a certain point. The minus signs indicate that the scanned surface is beneath the perfect cylinder surface and positive deviation indicates that the scanned surface is over the perfect cylinder surface. Based on the deviation measurements at the three major deviation zones it was concluded that the maximum high – low misalignment was 0.896 mm in magnitude.

### 1.4 MACHINING THE GIRTH WELD FLAW

For the first two experiments in the test matrix (Table 1), a flaw of 1.7 mm depth and 50 mm circumferential length is machined in two stages using blades of two different thicknesses. This flaw depth corresponds to 25% of the nominal pipe wall thickness (t). In the first stage the flaw is initiated using a jewelry blade of 0.012" thickness and cut up to a depth of 1.0 mm. In the second stage the blade is replaced with one of 0.006" thickness and the remaining 0.7 mm depth of the flaw is cut. Before starting to cut the flaw it is checked with an L-shaped ruler that the pipe surface is perfectly perpendicular to the blade. Afterwards the first 1.0 mm of the flaw is cut in 20 steps. In each step the depth of the flaw is increased 0.05 mm. In order to cut the flaw in circumferential direction, the pipe is rotated 50 mm using the rollers of the pipe stand in the opposite direction of the rotation direction of the blade.

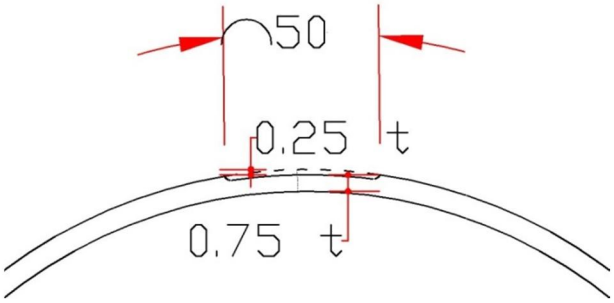


**Figure 8: Flaw dimensions (circumferential) [mm]**

The flaw machining equipment (Figure 10) consists of an x-y table (G1), an air driven motor which rotates the blade (G2), dial indicators showing the parallel to the pipe (G3) and perpendicular to the pipe (G4) position of the x-y table and a steel block (G5) clamped with the x-y table and holding the blade. The two red magnets on the pipe indicate the starting and ending points of the flaw in the circumferential direction. The depth of the flaw is controlled with the help of dial indicators (Figure 10) in the directions parallel (G1) and perpendicular (G2) to the pipe. The main function of the dial indicator G1 is to adjust the alignment of the blade in the direction parallel to the pipe during the process of replacing the 0.012" thick blade with the 0.006" one. In this process after the replacement of the new blade, the x-y table has to move to the left side 0.003" such that the blade stays aligned with the mid-line of the flaw as shown on the right hand side profile in Figure 9. It should be noted that both profiles are expected to have the same effect on the behavior of the pipeline, however, the symmetric profile was chosen.

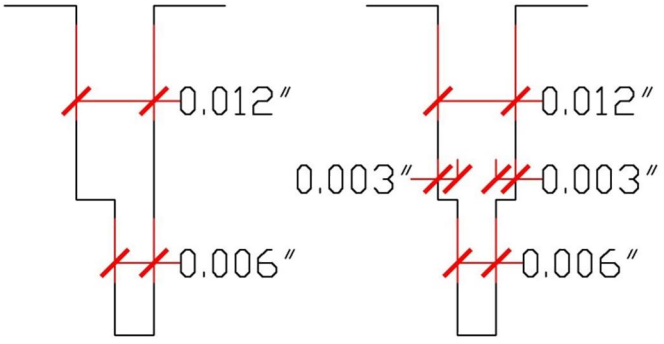


**Figure 9: Flaw dimensions (depth), undesired (left), desired (right)**

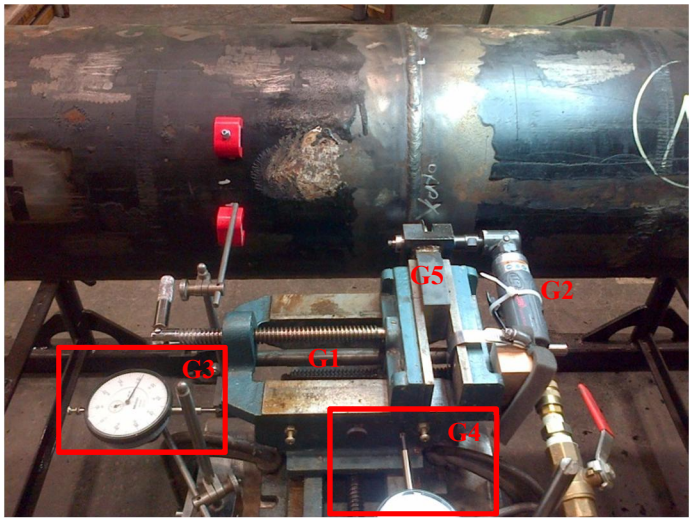


**Figure 10: Flaw machining setup**

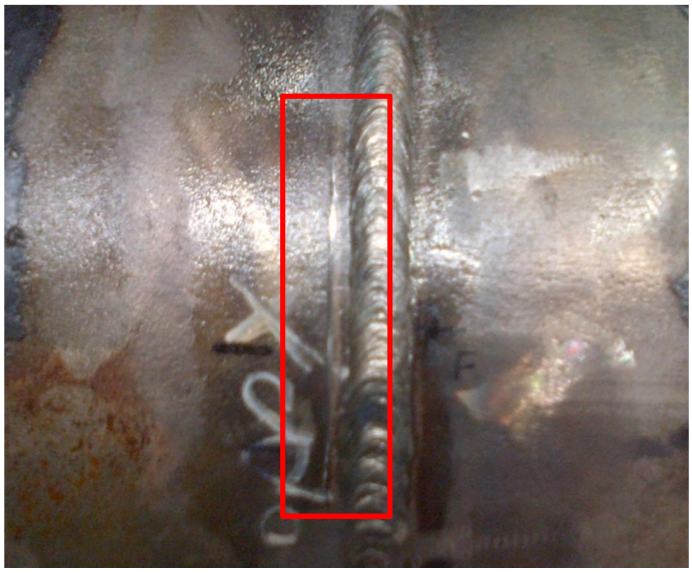

**Figure 11: Flaw of 50 mm length and 1.7 mm depth machined into the heat affected zone**

## 2. PREPARATION OF THE FULL SCALE SPECIMEN

In this section the details of the data measurement methods are explained. The main source of information in these tests is the measured strain and internal pressure data as well as the reaction force and displacement measured by the MTS machine. For the collection of strain data strain gauges and digital image correlation techniques are utilized. Also clinometers attached to the top and bottom end plates measured the rotation of end plates throughout the test. This rotation was caused by the eccentricity of the applied load.

### 2.1 POSITIONING OF THE STRAIN GAUGES

The strain gauges are positioned such that the longitudinal strain values could be measured at the remote strain locations (1-OD away from the end plates) as well as in the vicinity of the girth weld flaw. Also the hoop strain is measured in the mid-sections of each side of the pipe with circumferential strain gauges. Due to the eccentricity of the applied displacement the strain values were expected to differ along the circumference of the pipe. Positive longitudinal strain values were expected at the side of the pipe aligned with the flaw whereas compressive strain was expected on the opposite side. On the other hand the exact transition profile from tensile strain to compressive strain along the pipe circumference should be measured. For this purpose the pipe circumference is divided into four quarters (Figure 12) and at each quarter strain gauges are installed.

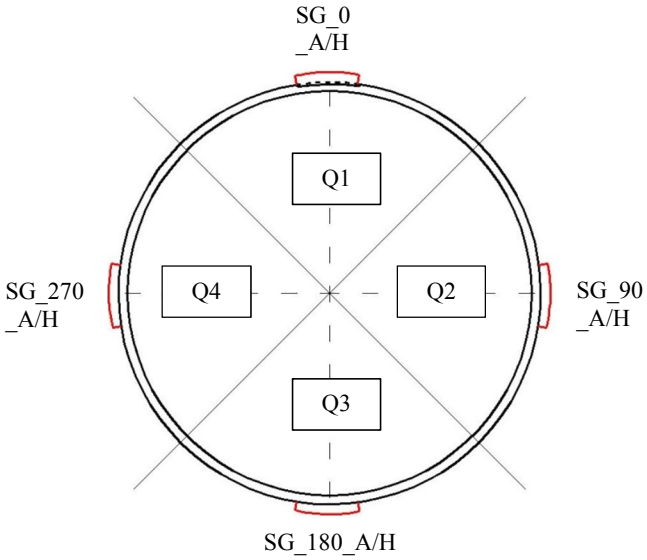


**Figure 12: Strain gauge positions around the pipe circumference**

These quarters are denoted with Q1 to Q4. The red lines on the pipe surface in the middle of each quarter show the location of the applied strain gauges. These lines are separated 90 degrees from each other and are denoted according to their angular distance from the flaw. Also the last letter in each strain gauge name indicates the direction of the strain gauge. For example SG_0_A is the strain gauge which is aligned with the flaw and measures the axial (longitudinal) strain. Similarly SG_90_H is the strain gauge which is located in a clockwise direction 90 degrees away from the flaw and measures the hoop strain at the side of the pipe. In the strain gauge setup the gauges 180 degrees away from the flaw are on the compression side of the pipe and expected to measure compressive strains whereas the gauges 0 degrees away from the flaw are measuring tensile strain values. The main function of the hoop strain gauges is to measure the circumferential expansion of the pipe due to the increasing internal pressure. However the main purpose of these experiments is to investigate the axial tensile strain capacity of the specimens. Therefore hoop strain gauges are applied only at the mid-sections of the pipe.

In order to capture the remote strain, also the gauge setup of Figure 12 is applied although this time the hoop strain

gauges are omitted. For this purpose axial strain gauges are installed on the top side of the pipe 1-OD away from the end plate. At the bottom side of the pipe the remote strain is captured using digital image correlation. The location of the remote strain is in compliance with the definition of remote strain in [10].

The amount of eccentricity of the applied displacement (0.1-OD) as well as the remote strain location can be seen in Figure 13. The amount of eccentricity of the tongue pieces is identical on both sides of the pipe. Also the pipe lengths on both sides of the girth weld are identical. Using this symmetry, only half of the specimen is shown in Figure 13.

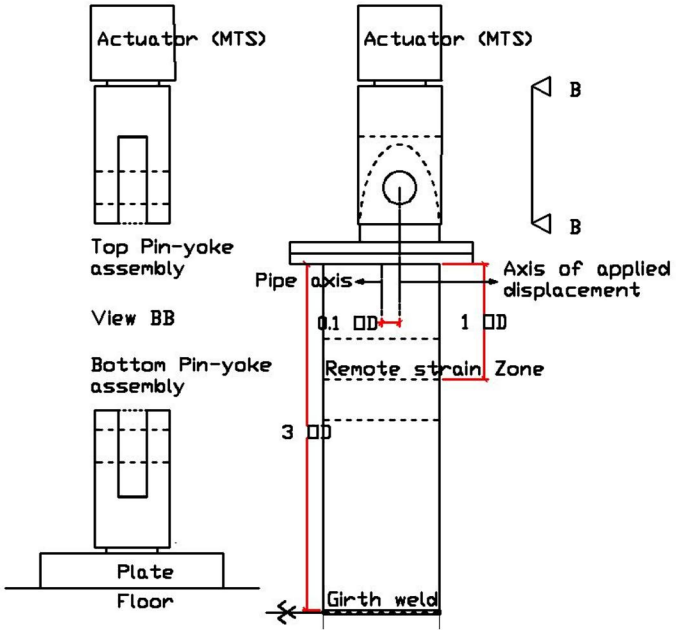


**Figure 13: Setup of the experiment**

On both ends of the pipe there are fixture plates with tongue pieces. The fixture plates are connected to the end plates with bolts of 1inch diameter. These bolts are pre-tensioned before the test using an impact wrench such that any elongation of the bolts due to the applied displacement is excluded from the test results. The tongues are attached to the end plates with fillet welds and have circular holes in them with diameters slightly larger than that of the pin. Also the thickness of the tongue is slightly less than the width of the opening of the yoke. In this way the pin can slide into the tongue once it is inside the yoke, building a pin-yoke assembly (Figure 13). The pin yoke assembly at the top side of the specimen is threaded into the actuator of the MTS machine which applies the displacement. At the bottom side the pipe is connected to the floor with another pin- yoke assembly which is threaded into a plate and this plate is bolted to the floor.

## 2.2 APPLYING THE INTERNAL PRESSURE

The internal pressure causing 80%SMYS hoop stress was calculated based on the nominal pipe dimensions (See section 1). In order to apply the internal pressure, the pipe is filled with water from a hole at the bottom end plate. Another hole at the upper end plate provides an air outlet so that no air is trapped inside the pipe during the tests. This air outlet is closed with a ball valve once the pipe is filled with water. An air driven pneumatic pump with a pressure capacity of 67.6MPa (9800PSI) is connected between the bottom end plate and the municipal water supply. Also an automatic pressure relief valve is connected to the water inlet of the bottom end plate which would release water as soon as the internal pressure exceeds the desired value for each test.

**Figure 14: Air -driven pneumatic pump**

## 2.3 MEASURING THE BENDED PROFILE OF THE SPECIMEN

Due to the eccentricity of the applied displacement, the initially straight pipe axis became curved during the experiment. In order to measure the development of this curvature, cable transducers are connected to the pipe at five different locations in the longitudinal direction. For this purpose an I – profiled steel column is placed approximately 1 m away from the pipe. The steel column and cable transducers are located on the side of the pipe which bends in compression. The cable transducers are connected to the steel column with magnets (Figure 15). In order to connect the cables to the pipe, nuts are glued on the pipe surface using epoxy and eye bolts are screwed into these nuts. The loops of the eye bolts are connected to the cables of the transducers using strings after pulling the cables about 6”. These strings and the cable transducers are enclosed in red boxes in Figure 15.

## 3. FULL SCALE TESTING PROCEDURE AND ITS RESULTS

In this section the procedure of testing the specimen is explained. Afterwards the load –displacement response of the tests 1 and 2 are presented and compared to the response predicted by the finite element analysis. The strain measurements of four different strain gauges at the remote strain zone are illustrated. The measured values of the hoop strain at the mid-section of the top side of the pipe are compared with the theoretical hoop strain values during the process of increasing the internal pressure.

Before applying any displacement to the specimen, the internal pressure is increased to the desired value in 1.4MPa (200PSI) increments. During the pressurization process the motion of the pipe in the axial direction was unconstrained so that the axial force applied by the MTS machine was zero throughout pressurization. It should be noted that the actual applied internal pressure fluctuated and the pump was used to increase the pressure whenever it decreased beyond the desired value. The actual applied average internal pressures were around 11.6MPa (1683PSI) and 3.48MPa (504PSI) for the first and second tests respectively.

Once the desired internal pressure was reached, the displacement was applied in a monotonic way at a rate of 0.2 mm/min up to a total displacement of 14.7 mm (1655kN reaction force). This amount of displacement caused the overall stiffness of the pipe to decrease significantly.

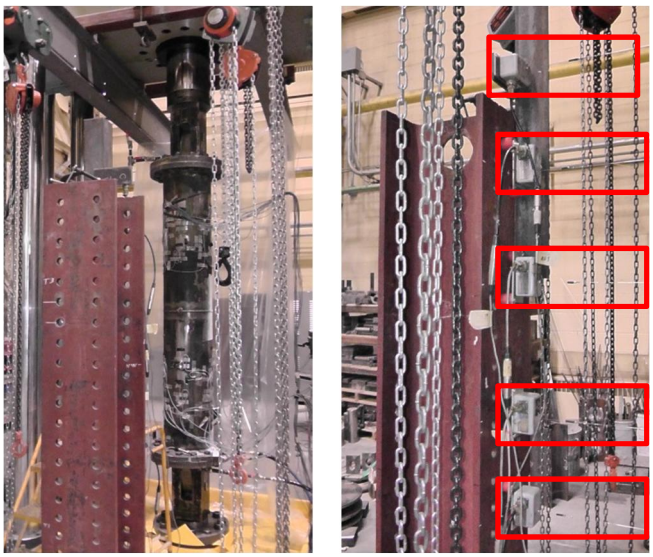

**Figure 15: Steel column and cable transducers**

**Figure 16: Flaw after rupture**

Since after the elastic limit the pipe is expected to exhibit more ductile behaviour, at this point the rate of applied displacement is doubled to 0.4 mm/min. In the nonlinear global response zone the rate of displacement was doubled two more times at 26.3 mm (1890kN reaction force) and 50mm (2200kN reaction force) total displacements up to a rate of 1.5 mm/min. Throughout the test the measurements are recorded every $10^{th}$ second. At a total axial displacement of 62.22 mm and a reaction force of 2339.4kN the pipe of test 1 burst at the flaw location due to crack propagation. Figure 16 shows the crack opening after the rupture. After the rupture the pipe was unloaded and a permanent displacement of 52 mm was observed. For the second test, the pipe exhibited a more ductile behaviour and the reaction force at failure was 3105kN. It should be noted that in the second test, the original tongue designed for this experiment exhibited large plastic deformation when the load exceeded 2600kN which prevented us from relying on the displacement recorded by the MTS actuator beyond that value. A total of 22mm of permanent displacement in the tongues was recorded at the end of the test. It is important to note that this displacement does not affect the recorded load or the measured strain values throughout the test. In addition, during the second test, as the load was higher than we had anticipated, the experiment was stopped to check on the safety of the hydraulic equipment. During that period, the load decreased which explains the dip in the load displacement curve (Figure 17) and the CMOD curves of the second experiment (Figure 18).

### 3.1 COMPARISON WITH THE FINITE ELEMENT ANALYSIS

The development of the reaction force at the loading pin during the entire experiment is compared to the result of the finite element analysis for both experiments in Figure 17. For the Finite element analysis, the load was applied in two steps. In the first step, the value of the actual experimental internal pressure was applied on the internal surface of the pipe and the end plate. In the second step, the maximum force reached in the experiment was applied on the loading pin. Due to symmetry, the resulting values of load and displacement were multiplied by two and compared with the results of the test (Figure 17).

It can be observed that the finite element for both experiments exhibit a stiffer response. While the slope of the nonlinear curves for both test 1 and test 2 match the slope of the corresponding models, the actual displacements of the test are much higher than the ones exhibited in the FEA. One of the reasons could be that the finite element model did not account for any deformation in the loading system (tongue and pin-yolk assembly) while in our second test we observed permanent deformation in the tongue of around 22mm (see section 3). Also in the numerical model the effect of stress intensity at the crack tip was ignored. In the actual experiment this stress intensity leads to a rapid crack propagation and fracture once the critical strain level was reached. The rapid crack growth towards the end of the experiment can also be observed from the development of the crack mouth opening displacement

(CMOD). To plot CMOD versus the applied load and displacement, the difference between the position of two points on both sides of the flaw, initially 28mm away from each other for both tests, is obtained using digital image correlation (Figure 18). The same curves were obtained if the initial distance between the points is 12.1mm(test 1) or 34mm (test 2). Both graphs show that CMOD at the onset of rupture is equal to 2mm. The two graphs clearly show a significant effect due to the internal pressure which is the sole difference between test 1 and test 2. While both curves have the same shape, the applied force and applied displacement that cause the unstable crack extension are much lower for the 11.6MPa internal pressure case (test 1) compared to the 3.48MPa internal pressure case (test 2).

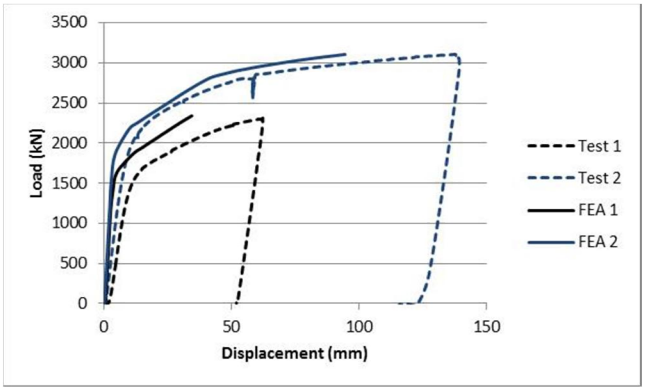


**Figure 17: Variation of the reaction force during the experiment (dashed) and in the finite element model (solid)**

### 3.2 AXIAL STRAIN MEASUREMENTS

The axial strain is measured 1.5-OD away from both end plates with four different axial strain gauges with 90 degrees angular intervals (Figure 19 and Figure 20). The pipe exhibited a ductility that is higher than expected. The strain gauges at areas were the strain increased more than 3.4% failed beyond that value. In addition, two strain gauges stopped recording strain beyond around 1% (Figure 19a). However, the comparison between the measurements in the top quarter and bottom quarter of the pipe show that the top and bottom parts of the pipe exhibited the same distribution of strain as the load was applied. In addition, the strains predicted from the FEA were in good agreement with those predicted by the strain gauges up to the point at which the strain gauge stopped collecting data. In order to compare the critical strain between test 1 and test 2, the digital image correlation technique which does not have a limitation on the maximum strain is used to report the strain at 225mm and 700mm away from the girth. At 225mm away from the girth weld, the strain at failure was around 2.2% for test 1 and 5% for test 2. At 700mm away from the girth weld, the strain at failure was around 4.8% for test 1 and 10% for test 2. This indicates that the internal pressure alone causes more than 50% decrease in the critical strain associated with the crack used in this set of tests.

### 3.3 COMPARISON OF THEORETICAL AND EXPERIMENTAL HOOP STRAIN VALUES

Under the assumptions of a plane stress condition and isotropic material behaviour, the hoop strain ($\varepsilon_h$) at the end of the pressurization step can be expressed as follows:

$$\varepsilon_h = \frac{1}{E}(\sigma_h - \nu\sigma_l) \tag{3.3.1}$$

Using the definition of $\sigma_h$(hoop stress) and $\sigma_l$ (longitudinal stress) as functions of $p_i$(internal pressure), $OD$ and $t$, equation (3.3.1) becomes

$$\varepsilon_h = \frac{1}{E}\left(\frac{p_i \cdot OD}{2t} - \nu\frac{p_i \cdot OD}{4t}\right) \tag{3.3.2}$$

Using (3.3.2), the theoretical hoop strain values and their differences from the experimental values at every internal pressure increment are tabulated in Table 3.

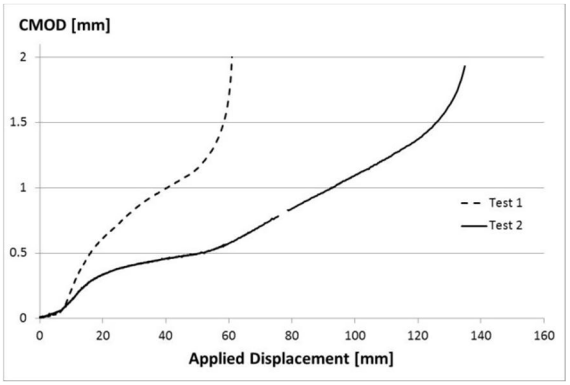


(a)

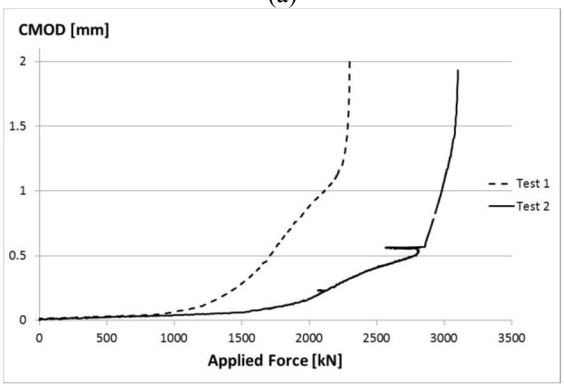


(b)

**Figure 18: Variation of CMOD (a) with respect to the applied displacement (b) with respect to the applied load.**

In Table 3 the experimental hoop strain value is calculated taking the average of four strain gauge measurements in the hoop direction at the mid-section of the top side of the pipe (Test 1). For test 2, one of the strain gauges was faulty and another one was not properly zeroed before the experiment, so, the experimental hoop strain is obtained by taking the average of three strain gauge measurements in the hoop direction. Two of them were at mid length of the top side of the pipe and one was at 1-OD away from the end plate. The theoretical hoop

strain was always higher than the experimental strain but the difference monotonically decreased with the increase in the internal pressure. The differences at the maximum applied pressure were around -2.3% and -0.93% for tests 1 and 2 respectively. One of the main reasons is that at smaller internal pressures, the Barlow formula exaggerates the stresses due to the internal pressure since the OD is used to calculate the stresses. As the pressure increases and the pipe expands, the Barlow formula gives better approximations for the stresses due to the internal pressure.

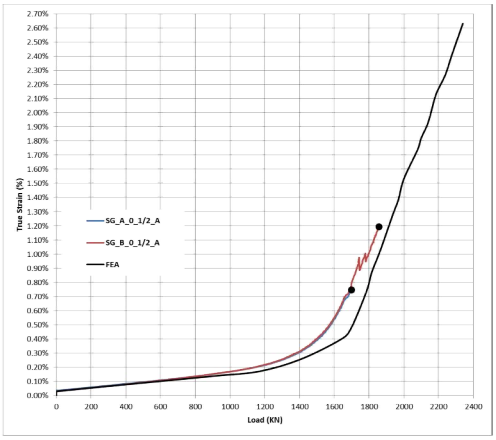


(a)

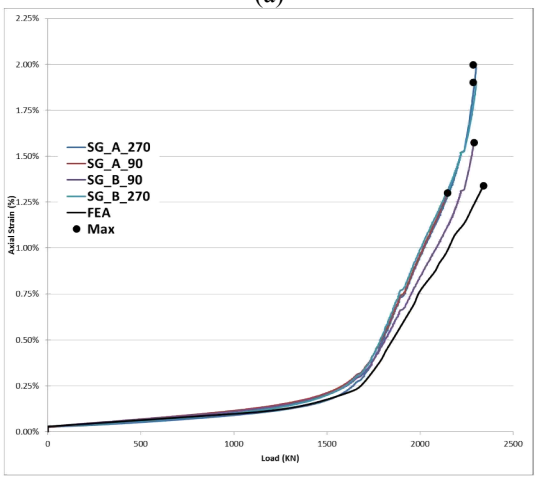


(b)

**Figure 19: Test 1. Comparison between axial strain gauge measurements and the FEA at the top (designated A) and bottom (designated B) one quarter of the pipe top (a) aligned with the crack, (b) at 90 and 270 degrees**

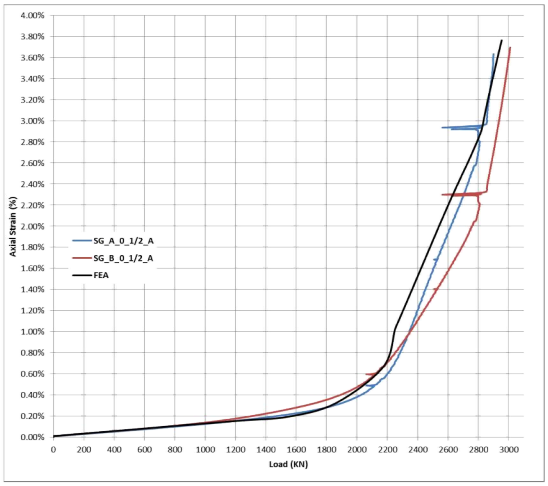


(a)

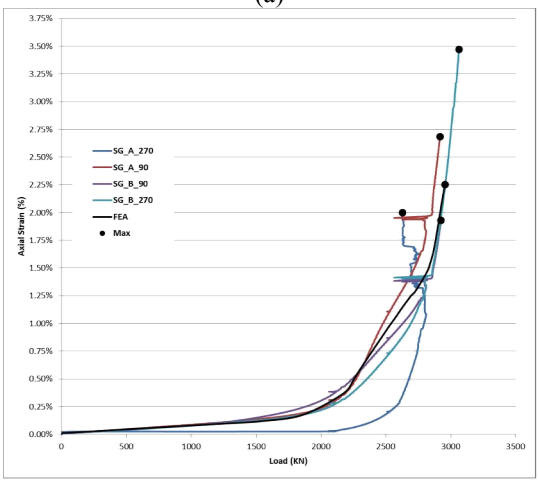


(b)

**Figure 20: Test 2. Comparison between axial strain gauge measurements and the FEA at the top (designated A) and bottom (designated B) one quarter of the pipe top (a) aligned with the crack, (b) at 90 and 270 degrees**

**Table 3: Comparison of theoretical and experimental hoop strain values for tests 1 and 2 after pressurization**

| Test 1 | | | | |
|---|---|---|---|---|
| Internal pressure | | Hoop strain (microstrain) | | |
| PSI | MPa | Experimental | Theoretical | % diff |
| 53.46 | 0.37 | 33.65 | 36.50 | -7.81 |
| 185.10 | 1.28 | 116.79 | 126.37 | -7.58 |
| 315.15 | 2.17 | 199.87 | 215.16 | -7.10 |
| 604.14 | 4.17 | 388.31 | 412.45 | -5.85 |
| 1013.06 | 6.98 | 661.70 | 691.63 | -4.33 |
| 1202.55 | 8.29 | 790.80 | 820.99 | -3.68 |
| 1402.61 | 9.67 | 925.08 | 957.58 | -3.39 |
| 1590.59 | 10.97 | 1055.31 | 1085.91 | -2.82 |
| 1697.85 | 11.71 | 1132.23 | 1159.14 | -2.32 |
| Test 2 | | | | |
| 61.20 | 0.42 | 32.17 | 41.78 | -23.01 |
| 244.83 | 1.69 | 160.36 | 167.15 | -4.06 |
| 451.98 | 3.12 | 304.41 | 308.57 | -1.34 |
| 497.84 | 3.43 | 336.71 | 339.88 | -0.93 |

## 4. DISCUSSION AND CONCLUSIONS

In the strain based design of pipelines the presence of possible girth weld defects plays a significant role. Extensive research is done in the recent years in order to better understand the effect of different crack sizes in the vicinity of girth welds on the tensile strain carrying capacity of pipelines. Girth weld locations may be considered as one of the relatively weaker parts of the pipeline structure. This weakness is mainly due to the presence of heat affected zones around the girth weld and the possible presence of imperfections. The research projects conducted to date mainly investigated the tensile behaviour of high strength steel pipes of grades X65 and higher. These research projects involved not only testing of curved wide plates cut out of line pipes but also testing of full scale specimens in the presence of internal pressure. The results of these experiments combined with parametric finite element analyses provided valuable insight in the estimation of the tensile strain capacity of high strength steel pipes. These results are used in order to formulate the strain response of high strength steel pipes in the presence of girth weld flaws as a function of pipe material properties, pipe geometry and girth weld flaw size.

Currently closed form equations are available in the CSA code for the design of pipeline systems (Z662-11), which can provide predictions for the estimation of the tensile strain capacity of steel pipes. These equations were based on experimental work on pipes having steel grade higher than X65. It is not clear how applicable these equations are to pipes with the steel grade X52. Also the effect of internal pressure is not included in these closed form equations. Our paper augments the current experimental and numerical analysis by Wang et al [10]-[15] by investigating the tensile strain capacity of X52 pipes in the presence of internal pressure. For this purpose a full scale tests program is being carried out at the University of Alberta which involves the testing of full scale pressurized X52 pipe under eccentric displacement controlled loading. In this paper the preparation process of this full scale tensile strain experiment is elaborated. Also the results of the full scale test of the first two tests are presented based on both experimental data and finite element analysis. It was found that the X52 pipe with a crack of 50 mm length, $0.25t$ depth, and maximum operating pressure is capable of undergoing about 2.2% longitudinal strain at 225mm away from the crack before rupture occurs. When the internal pressure is decreased to around 30% of the maximum operating pressure, the pipe behaves in a very ductile manner and undergoes a longitudinal strain up to 4.8% at 225mm away from the crack.

On the other hand using the currently available tensile strain equation in CSA Z662 (Equation 1) for our pipe and crack configuration would yield an estimated $\varepsilon_t^{crit}$ that is independent of the internal pressure and is also much smaller than what was achieved in the experiment. For both tests, $\xi = 7.19, \eta = 0.25,$ and $\lambda = 0.695,$ where the latter was obtained from the actual stress strain curve of the material. The range of $\delta$ in the code is given between 0.1 and 0.3 resulting in $0.5\% \leq \varepsilon_t^{crit} \leq 1.63\%$ indicating that the code equation is highly conservative when applied to this pipe and crack configuration.

**Acknowledgement**

Partial funding for this study was provided by NSERC

## REFERENCES

[1] CSA Z662-11; Oil and gas pipeline systems - Sixth Edition; Update No. 1: January 2012

[2] Wang, Y-Y., Cheng W., Horsley D. (2004); "Tensile Strain Limits of Buried Defects in Pipeline Girth Welds" Proceedings of IPC2004, International Pipeline Conference, IPC2004-524

[3] Wang, Y-Y., Chen, Y. (2005); "Reliability Based Strain Design" Gas Research Institute Report 04/0146. Des Plaines, IL.

[4] Wang Y-Y., Cheng, W. (2004); "Guidelines on Tensile Strain Limits" Gas Research Institute Report 04/0030. Des Plaines, IL.

[5] Wang Y-Y., et al (2004); "Tensile Strain Limits of Girth Welds with Surface-Breaking Defects, Part 1 – An Analytical Framework" Proceedings of the 4th International Conference on Pipeline Technology, 235—249

[6] Wang Y-Y., et al (2004); "Tensile Strain Limits of Girth Welds with Surface-Breaking Defects, Part 2 – Experimental Correlation and Validation" Proceedings of the 4th International Conference on Pipeline Technology, 251 – 266

[7] Verstraete M., De Waele W., Denys R., Hertele S.(2012); "Comparison of Pipeline Girth Weld Defect Acceptance at the Onset of Yielding According to CSA Z662 and EPRG Guidelines" Proceedings of the 9th International Pipeline Conference IPC 2012-90593

[8] Verstraete M., De Waele W., Denys R., Hertele S.(2012); "Pressure Correction Factor for Strain Capacity Predictions Based on Curved Wide Plate Testing" Proceedings of the 9th International Pipeline Conference IPC 2012-90592

[9] Cakiroglu C., Duke K., El-Rich M., Adeeb S., Cheng J.J.R., Sen M.(2012); "Influence of Girth Weld Flaw and Pipe Parameters on the Critical Longitudinal Strain of Steel Pipes" Proceedings of the 9th International Pipeline Conference IPC 2012-90736

[10] Wang, Y.-Y., Liu, M., Long, X., Stephens, M., Petersen, R., and Gordon, R. (2011); "Validation & Documentation of Tensile Strain Limit Design Models for Pipelines," US DOT Contract No. DTPH56-06-T000014, final report, http://primis.phmsa.dot.gov/matrix/PrjHome.rdm?prj=200

[11] Wang, Y.-Y., Liu, M., Zhang, F., Horsley, D., and Nanney, S. (2012); "Multi-tier tensile strain design models for strain-based design Part I - fundamental basis," Proceedings of the 9th International Pipeline Conference, Calgary, Alberta, Canada, September 24-28.

[12] Liu, M., Wang, Y.-Y., Song, Y., Horsley, D., and Nanney, S. (2012); "Multi-tier Tensile Strain Models for Strain-Based Design Part II - Development and Formulation of Tensile Strain Capacity Models," Proceedings of the 9th International Pipeline Conference, Calgary, Alberta, Canada, September 24-28.

[13] Liu, M., Wang, Y.-Y., Horsley, D., and Nanney, S. (2012); "Multi-tier tensile strain design models for strain-based design Part III - model evaluation against experimental data," Proceedings of the 2012 9th International Pipeline Conference, Calgary, Alberta, Canada, September 24-28.
[14] Wang, Y.-Y. and Liu, M., (2013); "Status and Applications of Tensile Strain Capacity Models,, Proceedings of the 6th Pipeline Technology Conference, Ostend, Belgium, October 7-9.
[15] Wang, Y.-Y., Liu, M., and Song, Y., (2011); "Second Generation Models for Strain-Based Design," US DOT Contract No. DTPH56-06-T000014, final report, http://primis.phmsa.dot.gov/matrix/PrjHome.rdm?prj=201